Journal Name

ARTICLE TYPE

Cite this: DOI: 10.1039/xxxxxxxxxx

Permeation Pathways through Lateral Domains in Model Membranes of Skin Lipids†

Annalaura Del Regno*[a‡] and Rebecca Notman*[a]

Received Date
Accepted Date

DOI: 10.1039/xxxxxxxxxx

www.rsc.org/journalname

An understanding of how molecules permeate the complex lipid matrix of the stratum corneum (SC) skin barrier is important for transdermal drug delivery, preventing the adsorption of toxic chemicals and tackling skin diseases. In this paper we present atomistic molecular dynamics simulations of skin-lipid bilayers composed of ceramides, cholesterol (CHOL) and free fatty acids at different lipid compositions and levels of hydration and investigate both perpendicular and lateral permeation pathways through the systems. We show that in fully hydrated bilayers the lipids are heterogeneously distributed, with CHOL-rich domains emerging spontaneously during the simulations. Potential of mean constraint force calculations reveal that the most favourable permeation pathway for water in the direction normal to the bilayer is through a CHOL-rich region, probably due to the disordering effect of CHOL on lipids in the gel-phase. In systems with a low water content (akin to real skin) we find that rather than forming continuous layers, water forms flattened ellipsoid-shaped pools between the lipid headgroups, which are separated by dry regions. This implies that there is no continuous aqueous lateral pathway in the SC and may help to explain why skin is such an effective barrier. We propose that the most probable permeation pathway for a small polar molecule consists of hopping from the headgroup region of one bilayer to the next via a dry region, followed by permeation along the bilayer normal through a CHOL-rich region to the centre of the bilayer where it can diffuse laterally in the lower-density lipidic environment before encountering another CHOL-rich region through which it can exit the bilayer.

1 Introduction

The topmost layer of skin (the stratum corneum or SC, Figure 1a) forms the main physical barrier against water loss from inside the body and penetration of exogenous substances from the external environment. The SC is often described as a "bricks and mortar" arrangement[1] (Figure 1b) whereby keratin-enriched cells called corneocytes (the "bricks") are surrounded by layers of intercellular lipids (the "mortar")[2]. The lipid lamellae are thought to provide skin with most of its barrier properties; thus they are important targets for strategies to reduce or enhance the skin barrier, e.g. for transdermal drug delivery or to protect against the adsorption of hazardous substances.

The lipid composition of the SC is very heterogeneous and rather unusual compared to that of typical cell membranes, which predominantly comprise phospholipids. The main lipid classes in the SC are ceramides, cholesterol (CHOL) and free fatty acids, at approximately equimolar ratio[4], with small amounts of cholesterol sulfate and cholesterol esters[2]. Ceramides consist of a sphingoid base amide-linked to a fatty acid. There are at least 12 different types of ceramide that differ in the molecular structure of the polar headgroup[5]. In addition, the fatty acid moiety of the ceramide may range in length from 12 to 32 carbon atoms[6]. The most abundant ceramide in the SC is CER[NS]24[7], which has a sphingosine backbone with 18 carbon atoms and a non-hydroxy fatty acid tail of 24 carbon atoms (Figure 1c). Likewise, there is polydispersity within the free fatty acid family, with the most abundant free fatty acid in the SC (FFA24) also characterised by a 24 carbon atom chain[8] (Figure 1c).

It is well-established that the SC lipids are organised in lamellar sheets[9] that allow for minimal water loss while retaining flexibility and resistance under bending and lateral stress. However, despite over 30 years of effort, the molecular organisation of the lipids, both within the sheets and from one sheet to the next is still not well understood. Experimentally it has been observed that

[a] Department of Chemistry, University of Warwick, Gibbet Hill Road, Coventry, CV4 7AL, United Kingdom. E-mail: a.del-regno@warwick.ac.uk, r.notman@warwick.ac.uk

† Electronic Supplementary Information (ESI) available: [Bilayer set-up, Structural properties, 2D thickness and number density maps for the models, Cluster analysis, Details of the water pools, Bilayer compositions versus permeability and resistance, Potential of mean force and diffusion versus the systems' density profiles]. See DOI: 10.1039/b000000x/

‡ Present address: STFC Hartree Centre, SciTech Daresbury, Warrington, Cheshire WA4 4AD, United Kingdom. E-mail: annalaura.del-regno@stfc.ac.uk

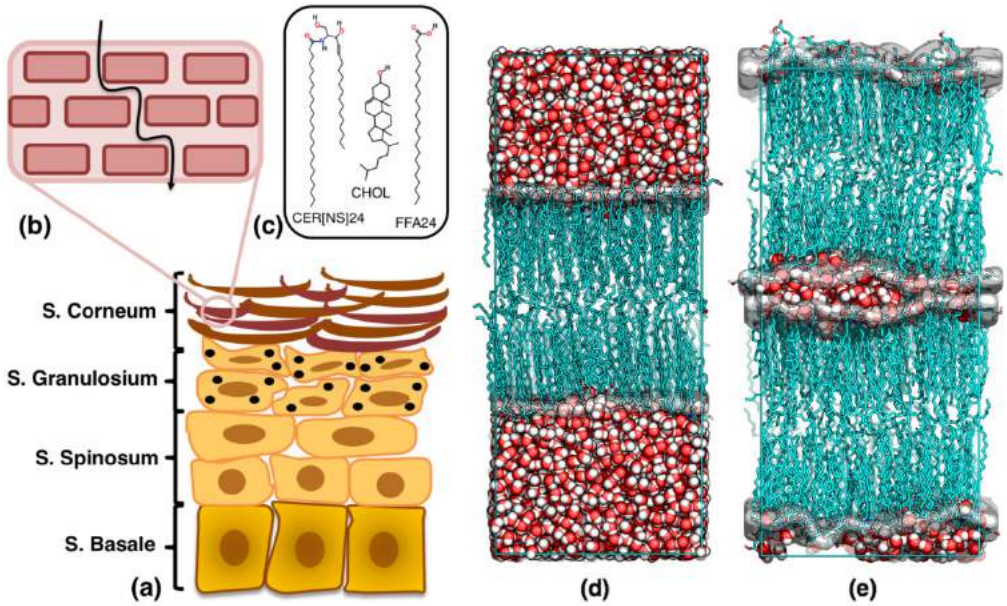

Fig. 1 (a) Schematic representation of the epidermal layers adapted from Krieg and Füstemberger[3]. (b)"Bricks and mortar" model of the SC; the black arrow indicates a possible pathway of permeation through the lipid lamellae. (c) Main components of the SC lipid lamellae used in this work. Snapshots of (d) FH and (e) LH bilayers after 47 ns of MD simulation. Water molecules are shown as spheres and lipid molecules as sticks. Carbon is coloured in cyan, oxygen in red, hydrogen in white and nitrogen in blue. The surfaces defined by the lipid headgroups are shown in grey.

there are two coexisting lamellar phases[4,5,10–13] (the short and long periodicity phases[2,10,11]). Furthermore most of the lipids are packed in a dense orthorhombic arrangement with some slightly-less-dense hexagonally packed and much-less-dense fluid-phase lipids[14]. Attempts to explain these findings have led to the proposal of a number of different models[15] such as the "sandwich model", where crystalline lipid bilayers are separated by a thin layer of partially fluid lipids[2] and the "domain-mosaic model", where lipids in the gel/crystalline phase are separated by grain borders consisting of lipids in the fluid/liquid crystalline phase[16]. In general there appears to be a consensus that the lipids are not distributed homogeneously within the SC lamellae. Indeed, distinct domains have been observed using simple mixtures of skin lipids[17,18]. The implication is that domains of different lipid composition will have different macroscopic properties such as bending rigidity, lateral stress and permeability. Thus, in order to make accurate predictions about the adsorption and transport of molecules through skin or other mixed-lipid membranes, it may be necessary to consider the local, molecular-level, environment of the permeant rather than the bulk membrane composition. Furthermore, lipid domains in *cell* membranes may have a much broader biological significance, for example in the formation of functional compartments and in fundamental cellular processes such as cell signalling[19,20]. An understanding of domain formation may also assist in the development of novel stimuli-responsive materials where the lateral lipid organisation changes in response to some external stimulus, for example for use in drug delivery and as biosensors[21].

The water content of the SC also contributes to its overall permeability. Between 15 and 30% of the total mass of the SC is water[22], which is low compared to other biological tissues. A water gradient exists across the SC that is determined by the difference in relative humidity of the external environment and the more aqueous internal tissues[22,23]. More hydrated skin is more permeable[24], which may be correlated to changes in the mobility and phase behaviour of the lipids[25]. The distribution of water within the SC is not yet clear. Under normal conditions, most of the water is thought to be bound to keratin filaments within the corneocytes[26]; however there is a constant flux of water across the SC (that gives rise to transepidermal water loss), which suggests that water must also be located in the intercellular, lipidic region. The most obvious location for intercellular water is between the lamellar sheets, where it can interact with the polar lipid headgroups but this has yet to be demonstrated conclusively. When SC is highly hydrated to ∼300% w/w, the corneocytes swell and eventually become saturated and pools of water are observed in the intercellular space[26,27].

The complexity of the SC lipid lamellae presents a real challenge to the scientific community as it is difficult to determine the relationship between the molecular organisation of the lipids and bulk properties and the interactions of permeant molecules by experiments alone. Over the past 10 years molecular dynamics (MD) simulation has enabled us to start to rationalise the experimental picture of the SC and make predictions that can guide future studies[28–30]. Initial work focused on establishing models that reproduced the structure and phase behaviour of pure- and two-component skin-lipid bilayers in water[31–35]. This was followed by simulations of more complex mixtures of ceramides, CHOL and free fatty acids, which revealed how the ratio between different lipid classes contributes to the properties of the SC and explored the relationship between the polydispersity of the lipids and the overall packing and fluidity of the resultant membrane[36–42]. Additional simulation studies have explored the effect of additives such as ethanol[43], DMSO[32,44] and oils[45,46] and

have attempted to characterize the permeation of small molecules through homogeneous skin-lipid membranes[37,43,47].

In this work we characterize model membranes of CER[NS]24, CHOL and FFA24 at different levels of hydration and explore the lateral and perpendicular pathways of water across the membranes using atomistic MD simulations and potential of mean constraint force calculations. Our results indicate that the lipid species are heterogeneously distributed in the bilayer and that, rather than forming a continuous aqueous layer, water forms distinct pools between the bilayers. The implications of this are (i) that there a number of putative routes through the lipid membranes that differ in the local lipid composition and (ii) that there is no continuous aqueous lateral pathway between the lipid layers. Taking this into account and using key parameters , i.e. permeability and diffusion coefficients, determined from the simulations, we propose the most probable permeation pathway for water and other small polar molecules across the SC skin barrier.

2 Computational Methodology

2.1 Model Bilayer Systems

In this work we have modelled multicomponent skin-lipid bilayers with two different lipid compositions (CER[NS]24:CHOL:FFA24 ratios of 1:1:1 and 2:2:1) and two levels of hydration (fully hydrated FH, with a lipid:water ratio of 1:30 and low hydration LH, with a lipid:water ratio of 1:2). FH models are widely used in lipid bilayer studies[32,36–39,43,44,48]; they are simple to implement and can be compared with well-defined model lipid systems used in experiments and previous simulations. They may also be representative of the top layers of skin in contact with an aqueous phase. The LH systems, which have not previously been simulated, aim to provide a more realistic description of the dryer environment of the lipids in real skin, with a water content equivalent to that reported experimentally[5]. The FH models comprise a single lipid bilayer with an aqueous layer above and below both leaflets. In the LH models, a thin layer of water separates two bilayers stacked on top of each other. Snapshots of the two different bilayer systems after 47 ns of simulation are shown in Figures 1d and e and the exact molecular compositions are reported in Table S1 in the Supporting Information.

2.2 Forcefield Details

The interaction potentials and associated parameters for the lipids and water were identical to those used in previous works by us and others[32,36–39,43,44]. In brief, the interaction parameters used to describe CER[NS]24 and FFA24 tails were based on the united-atom force field of Berger[49]. This force field uses GROMOS87 parameters for headgroups and specially adapted OPLS parameters[50] for lipid tails; the dihedral potentials in the hydrocarbon tails are described by the Ryckaert-Bellemans term[51]. Partial charges are given in reference 36. The forcefield parameters for the polar part of the FFA24 and the CHOL were the same as those used by Höltje et al.[33]. The water molecules were described by the single point charge (SPC) water model[52].

2.3 Initial Configurations of the Bilayers

To build the model membranes we first constructed anhydrous bilayers with the desired lipid composition (ratio of CER[NS]24:CHOL:FFA24). A unit cell of 6 (for the 1:1:1 bilayer) or 10 (for the 2:2:1 bilayer) lipids, was replicated in the x and y directions to yield a bilayer of 90 lipids per leaflet. The initial structure underwent a semi-isotropic NPT MD simulation (Stage 1, Table S2) where the lipids were restrained in the z direction but allowed to move freely in the xy plane. After reaching a constant area per leaflet, a MD simulation was performed at elevated temperature in an attempt to enhance lateral mixing of the lipids and reduce the bias from their starting configuration, followed by a cooling stage to re-equilibrate the bilayer at skin temperature (Stages 2-3, Table S2). Water was then added to each system to generate FH or LH bilayers. For the FH models, 30 water molecules per lipid were randomly inserted above or below the bilayer. Following the addition of water, two stages of MD simulation were carried out consisting of a short equilibration and a final run of 47 ns (Stages 4b-5, Table S2). To create the LH models, two water molecules per lipid were added above a single anhydrous bilayer. A 2 ns NVT MD simulation was then run to allow the absorption of the water molecules at the lipids' surface (Stage 4a, Table S2. The simulation cell was then replicated in the z direction to obtain a multilamellar system and Stages 4b-5 (Table S2) performed on the resulting model. Unless indicated otherwise, analysis was carried out on the last 25 ns of Stage 5. For each of the four systems, three independent replicas were built which differed in the assignment of random initial velocities at the start of Stage 1 with all subsequent stages the same. In addition, a larger 1:1:1 LH system was prepared by taking one of the bilayers at the end of Stage 4 and replicating it in the x and y directions to obtain a 2×2 model bilayer, before continuing as for the smaller bilayers. Stage 5 in this case was extended to 425 ns.

2.4 Simulation Parameters

All simulations were performed using the Gromacs package version 4.5.4[53]. The temperature of lipids and water was controlled separately by a Nosé-Hoover thermostat with a time constant of 0.1 ps. The pressure was controlled by a Parrinello-Rahman barostat[54,55] with a time constant of 5 ps and compressibility of 4.5×10^{-5} bar^{-1}. Electrostatic interactions were calculated using the particle mesh Ewald method[56,57]. The cut-off distance for both the short-range part of the electrostatics and the van der Waals interactions was 1.2 nm. All lipid bonds were constrained using the LINCS algorithm[58] and water was treated as rigid using the SETTLE algorithm[59].

2.5 Free Energy Theory

To calculate the permeability coefficient of water in the bilayers, the potential of mean constraint force method was used. This method has been successfully employed to determine the partition coefficients of small molecules in DPPC bilayers[60–64] and more recently to assess the permeability of water through fully hydrated[37,43] and dehydrated[38] skin lipid bilayers. In this ap-

proach, the centre of mass (COM) of the permeant is constrained at a certain depth z in the lipid bilayer (along the bilayer normal direction) while it is able to move freely in the xy plane. At each step, the equation of motion is calculated without any constraint and then the atomic coordinates of the solute are corrected to satisfy the distance constraint between the COM of the solute and the bilayer. The force F_i required to maintain the constraint is calculated at each MD step and is equal to:

$$F_i = m_i \frac{\Delta z}{(\Delta t)^2} \tag{1}$$

where m_i is the mass of the solute, Δz is the displacement covered by the solute along the z axis while solving the equation of motion, and Δt is the simulation time step. The force $F(z,t)$ acting on the COM of the solute at a chosen z is equal to the negative of the force required to maintain the z-constraint. The free energy difference $\Delta G(z)$ is accessible as the potential of mean force (PMF) and is given by:

$$\Delta G(z) = \text{PMF} = -\int_{\text{outside}}^{z} \langle F(z')\rangle_t dz' \,. \tag{2}$$

Through the constraint method, dynamic properties of the system can also be calculated; the diffusion $D(z)$ of a solute in the lipid bilayer can be calculated from the friction coefficient $\acute{I}(t)$ at each time and depth according to:

$$D(z) = \frac{RT}{\acute{I}} = \frac{(RT)^2}{\int_0^\infty \langle \Delta F(z,t) \bullet \Delta F(z,0)\rangle dt} \tag{3}$$

where R is the gas constant and T is the absolute temperature. The permeability P of the solute can then be determined as the inverse of the overall membrane resistance R_m:

$$R_\text{m} = \int_{\text{outside}}^{z} \frac{\exp(\Delta G(\acute{z})/RT)}{D(\acute{z})} d\acute{z} = \frac{1}{P} \,. \tag{4}$$

Detailed descriptions of the method can be found elsewhere[37,60–63].

2.6 Free Energy Calculations

In this work, the permeability of water along the normal pathway was assessed for the 1:1:1 FH and LH systems. For the FH system, water molecules were considered moving from bulk water (the reference state) to the COM of the bilayer. For the LH system, water molecules were considered moving from the COM of one bilayer (the reference state) to the COM of the other.

The constrained water molecules were created at 0.2 nm intervals along the z direction of the bilayer. In the LH systems, additional independent simulations were carried out where the water molecules were created at 0.1 nm intervals at the interface between the two adjacent bilayers. The starting configurations were prepared by de-coupling the Coulombic and van der Waals interactions of a water molecule inserted at the desired z position within the lipid bilayer and gradually "switching-on" the interactions over a series of Langevin dynamics (LD) simulations (the coupling parameter (λ) for the water molecule was changed from 0 to 0.5 to 1 for LD simulations of 200, 300 and 400 ps respectively). This approach of "growing" the water molecules inside the bilayer avoided the potential pitfall of disrupting the bilayer by pulling the permeant though the membrane using an applied force. After the successful creation of the water molecules, an additional equilibration *NPT* MD simulation step was performed at 1 bar and 305 K for a total of 200 ps. The constrained simulations were then run for a total of 9 ns and F_z was collected every 0.1 ps. To calculate the diffusion through the bilayer, F_z was calculated every 0.001 ps for a total of 1 ns. The whole procedure was repeated nine times for both the FH and LH bilayers, where the water molecules were given different initial xy coordinates — thus nine different pathways along the z direction were explored for each system. To achieve better statistics, data were averaged over the equivalent z positions in the opposite or adjacent leaflet for FH and LH systems respectively.

2.7 Lateral Diffusion

In addition to permeation along pathways normal to the bilayer (considered above), permeation through the lipid lamellae may occur in the lateral directions i.e. in the plane of the bilayer. In order to investigate the nature of the most probable lateral pathways, two different scenarios were investigated: (i) permeation through the COM of the bilayers, where the lipid tail density is at its minimum, and (ii) permeation along the interface between two adjacent bilayers in the LH model, where the lipid headgroups reside. MD simulations of 40 ns at 305 K and 1 bar were carried out of a water molecule placed at the COM of the FH bilayer, at the COM of the LH bilayers and at the interface between adjacent bilayers in the LH system. Two runs for each scenario were collected, with different random initial velocities assigned to the atoms at the start of the simulation. The diffusion of the water molecule D_w was evaluated from the mean square displacement using the Einstein relation[65]:

$$\lim_{t\to\infty} \langle ||\mathbf{r}_\text{w}(t) - \mathbf{r}_\text{w}(0)||^2 \rangle = 6 D_\text{w} t \tag{5}$$

where $\mathbf{r}_\text{w}$ is the position of the water molecule and $\mathbf{r}_\text{w}(t) - \mathbf{r}_\text{w}(0)$ is the distance traveled by the water molecule over the time interval t.

2.8 Analysis

Bilayer thickness: The bilayer thickness as a function of the location in the xy plane of the bilayer was calculated using the g_lomepro package[66] developed for Gromacs[53]. The bilayer was mapped onto a 100 × 100 grid and each lipid assigned to a grid element. The thickness of a grid element was calculated as the difference between the top and bottom leaflet lipid coordinates along the direction normal to the bilayer and averaged over the last 1 ns of Stage 5, Table S2. The data are presented as 2D thickness maps.

Density maps: Number density maps of lipids in the xy plane were computed using the g_densmap tool in Gromacs and averaged over the last 1 ns of Stage 5, Table S2. As above, the box was divided into a 100 × 100 grid in the xy plane and the number density computed for each grid element.

Hydrogen bonds: Hydrogen-bonds (H-bonds) were defined using the geometrical criteria that a H-bond exists if the distance between the donor and the acceptor atoms is $\leq$ 0.35 nm and the acceptor-donor-hydrogen angle is $\leq 60^{\circ}$. The numbers of H-bonds were averaged over the last 25 ns of Stage 5, Table S2, and normalised by dividing the total number of H-bonds by the total number of lipids.

3 Results and Discussion

3.1 Structural Properties of the Bilayers

The focus of our work is on the lateral organisation and barrier properties of the lipid lamellae; nevertheless, to validate our models, key structural properties of the bilayers were calculated and are summarised in Table S3. A detailed description of the analysis methodologies and additional results (evolution of the structural properties over time and lipid tail order parameters) and discussion are also provided in SI. Overall we found that the structural properties of the bilayers are not strongly affected by the change in lipid composition or degree of hydration. Bilayers with higher concentration of CHOL than FFA24 (2:2:1 models) showed a slight increase in the disorder of the lipids, which is consistent with the well-known role of CHOL as a plasticiser of lipid membranes in the gel phase[67] and is in agreement with previous MD simulations of SC lipid lamellae[36]. This disordering is accompanied by an increase in the area per lipid and lipid tilting and a concomitant decrease in bilayer thickness. Lowering the water content has a similar effect on the bilayer structural properties although the mechanism is different and is likely due to an increased degree of tilting of the lipids (see Table S3) in an attempt to maximise H-bonding with the adjacent bilayer.

3.2 Lateral Distribution of Lipids

Fully hydrated bilayers: In a homogenous bilayer where the lipids are evenly distributed, a uniform thickness is expected over the entire structure. On the other hand, in a heterogenous membrane system that may contain domains or aggregates of different lipid species, one might observe variations in the bilayer thickness associated with the asymmetric lipid distribution. To probe the lateral distribution of lipids in the bilayers, 2D density and thickness maps were computed for each bilayer. The maps for a selected 1:1:1 FH bilayer are shown in Figure 2 (equivalent maps for the remaining samples can be found in Figures S8 and S9).

In all FH bilayers, there are variations in thickness of up to 1 nm between regions of low thickness ($\sim$4.0-4.1 nm, coloured blue/green) and regions of high thickness ($>$5.0 nm, areas coloured red). Number density maps of each component lipid in the *xy* plane are presented in Figure 2. It can be seen in both the 1:1:1 (Figure 2 and Figure S8) and 2:2:1 FH bilayers (Figure S9), that FFA24 tends to be distributed homogeneously within the bilayer whereas CHOL tends to form agglomerates with itself. This observation is supported by a cluster analysis of the different lipid species, which shows that FFA24 only forms transient clusters, whereas CHOL forms stable clusters that increase in size over the simulation (Figure S10-S12). The clusters do not tend to be circular in shape, rather CHOL forms a connected network that spreads throughout bilayer. A consequence of this is that there are regions of the bilayer that are locally-enriched and locally-depleted in CHOL. A snapshot showing a region enriched in CHOL is shown in Figure S13.

The formation of CHOL-rich regions in multicomponent lipid membranes has been widely observed both experimentally[68,70,71] and in simulations with forcefields different to the one used in our study (for example in simulations of mixed CHOL/FFA16 bilayers using the CHARMM forcefield[35] and phospholipid/CHOL mixtures using the MARTINI coarse-grained forcefield[69]. The driving force for CHOL aggregation may be due to favourable van der Waals interactions between the hydrophobic body of the CHOL molecules (H-bonding does not play a role as our analysis in Section 3.3 shows that CHOL does not form H-bonds with itself). Alternatively the predominant view in the literature is that phase separation of CHOL occurs in order to maximise the packing of the unsaturated alkyl tails of the other lipid components of the membrane.

As CHOL is shorter than CER[NS]24 and FFA24, one might expect that CHOL agglomerates would cause a local thinning of the bilayer that would explain the variations in thickness. However, a comparison of the CHOL density and thickness maps did not reveal a clear relationship between the local bilayer composition and the local thickness. To investigate this further the 2D thickness map was overlaid onto the final configuration of the bilayer, and the local composition inspected visually. The compositions of the bilayer in a low thickness region and a high thickness region are shown in Figure 3. At green low-thickness regions the composition is a mixture of FFA24 and CHOL molecules, where CHOL molecules are found embedded deeper in the bilayer compared to FFA24. In order to form hydrogen bonds with neighbouring molecules, FFA24 molecules are forced to bend away from a linear conformation, causing the reduction in thickness. The lowest values of the thickness (blue region of the 2D map) are due to the contribution of CHOL molecules which migrated to the centre of the bilayer (bottom right of Figure 3). In red high-thickness regions, FFA24 molecules adopt a straight conformation throughout the length of the leaflet. This appears to be due to a complementary packing of FFA24 with CER[NS]24. Indeed the presence of FFA24 in mixed CER[NS]/FFA24 bilayers partially increases the tail order of the CER molecules[36].

Low-hydration bilayers: The lateral thickness profiles and number density maps were also generated for the LH models. In these multi-lamellar models, each bilayer was analysed separately. A selected case is shown in Figure 4 and the equivalent maps for the remaining systems are provided in Figures S14-S24.

An even greater variation in bilayer thickness (of up to 1.4 nm) is observed in the LH systems than in the FH systems; here the membrane transitions between regions of low thickness of $\sim$4.0 nm (coloured blue) and regions of high thickness of $>$5.2 nm (coloured yellow/red). Despite this variation in

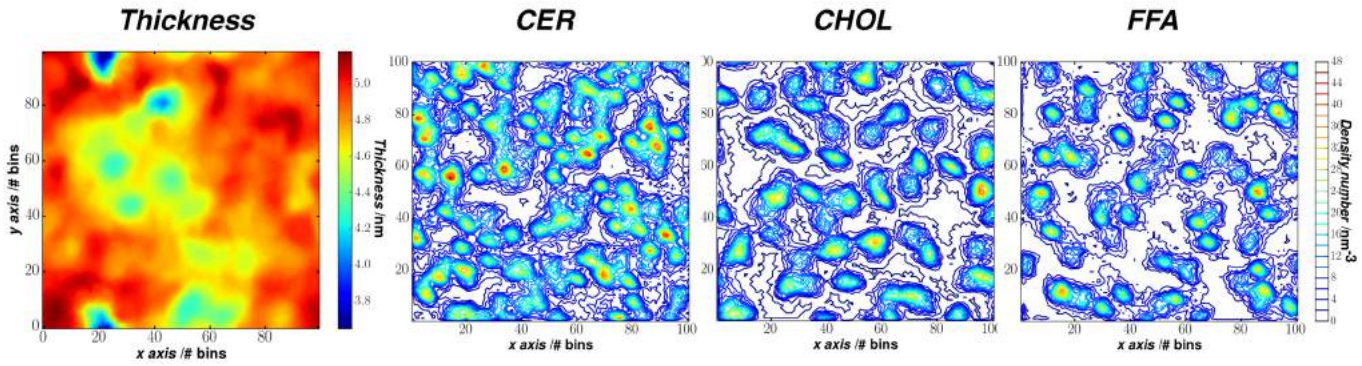

Fig. 2 Bilayer thickness as a function of position in the xy plane of the bilayer and corresponding 2D number density maps for CER, CHOL and FFA, for a selected FH 1:1:1 bilayer. Equivalent maps for all other systems can be found in Figures S8 and S9.

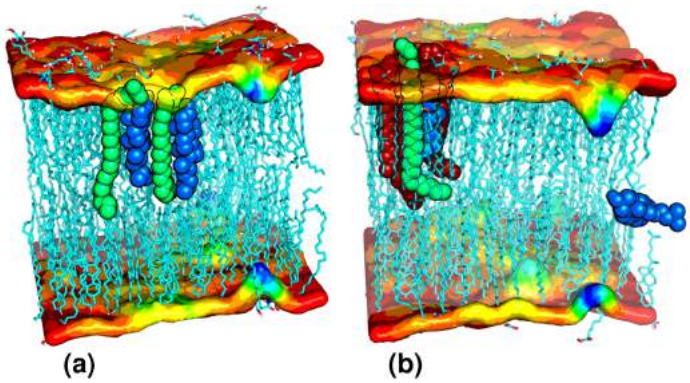

Fig. 3 Snapshot of a selected FH 1:1:1 bilayer with the corresponding 2D thickness map overlaid onto the bilayer surface. Left hand side: detail of the system around a low/medium thickness area. Right hand side: detail of the system around a high thickness area. Molecules in the areas of interest are represented by spheres. FFA24 molecules are coloured in green, CHOL molecules in blue and CER[NS]24 molecules in red. The remaining lipids are represented as sticks. Carbon is coloured in cyan, oxygen in red, hydrogen in white and nitrogen in blue.

thickness, comparison with the density maps shows that there is no clear phase separation between CHOL and FFA24 in the LH bilayers i.e. the lipid components appear to be evenly spread within the system, with no apparent formation of agglomerates. The lateral diffusion of the lipids in these systems is up to two orders of magnitude smaller than in the corresponding FH models (see Table 1), which we attribute to *inter*-layer H-bonds that are not present in the FH models.

Table 1 Lateral diffusion coefficients of lipids in the plane of the bilayer

CER[NS]24:CHOL:FFA24	D /cm^{2}s^{-1}	
(molar ratio)	FH bilayer	LH bilayers
1:1:1	$5.33(14) \times 10^{-5}$	$3.12(1) \times 10^{-7}$
2:2:1	$8.29(9) \times 10^{-6}$	$8.83(3) \times 10^{-7}$

In the LH systems, the variation in thickness is due to the formation of water pools on the surface of the membrane that induce a local deformation. Analyses of the H-bonds, lateral distribution of water and effect of pooling are discussed in detail below.

3.3 Hydrogen Bonding

The strong barrier properties of the skin lipids are attributed in part to the lateral H-bond network between lipid headgroups[32]; however it is not yet known how the H-bond network changes under conditions of low hydration. Furthermore, H-bond formation may be one of the driving forces governing the molecular organisation of the lipids and water. To investigate this further, the H-bond network of the bilayers was analysed by computing the numbers of lipid-solvent H-bonds, lipid-lipid *intra*-layer H-bonds (H-bonds between lipids in the same leaflet of the bilayer) and lipid-lipid *inter*-layer H-bonds (H-bonds between lipids in adjacent leaflets in a multi-lamellar system).

Our analysis of the H-bond network is presented in Figure 5. On the left hand side it is shown that the total number of H-bonds per lipid is $\sim$5 for both FH and LH bilayers. In the FH systems, where H-bonds between lipids can only occur in the lateral direction, this total comprises $\sim$1 lipid-lipid H-bond and $\sim$4 lipid-water H-bonds. Under conditions of low hydration, the lateral H-bond network is unaffected, however one of the lipid-solvent H-bonds (per lipid) is replaced by a inter-layer H-bond with the adjacent bilayer. A consequence of this is that by lowering the water content of the skin, the overall integrity of the multilamellar structure may be enhanced by the formation of stronger interactions between adjacent lipid layers. The presence of a H-bond network in the direction normal to the bilayer also reduces the lateral diffusion of the lipids (see Table 1 and discussed above), and explains why we do not observe CHOL-enriched and -depleted domains in the LH systems on the timescales of our simulations.

H-bonds involving lipids were sub-divided further to show the contributions from the different lipid species (right hand side of Figure 5). All the lipid species are involved to some degree with inter- and intra-layer H-bonds and in the formation of H-bonds with the solvent. H-bonding between lipid species in the plane of the bilayer (LIP-LIP intra) does not seem to be significantly affected by changes in lipid composition or hydration, which suggests that H-bonding is not the main driving force for the formation of aggregates. In terms of H-bonds between lipid layers,

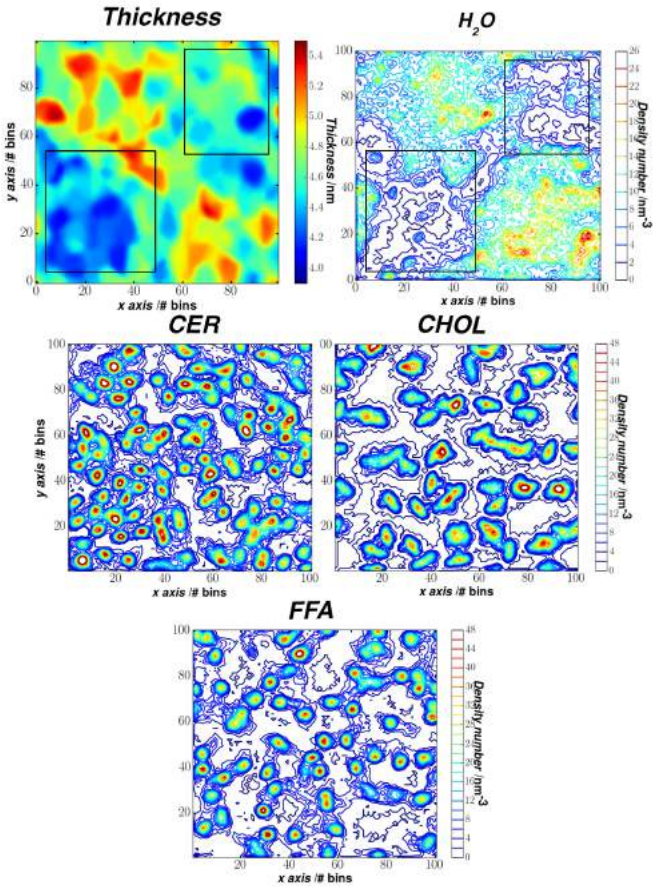

Fig. 4 Left hand side: (top) bilayer thickness as a function of position in the xy plane of one of the bilayers from a selected 1:1:1 LH model and number-density map of the inter-layer water. The black rectangles highlight areas of low thickness, which correspond to the dry regions of the bilayer. Left hand side: (bottom), number density maps for CER[NS]24, CHOL and FFA24 for the selected bilayer. Equivalent maps for all bilayers and all other systems can be found in Figures S14-S24.

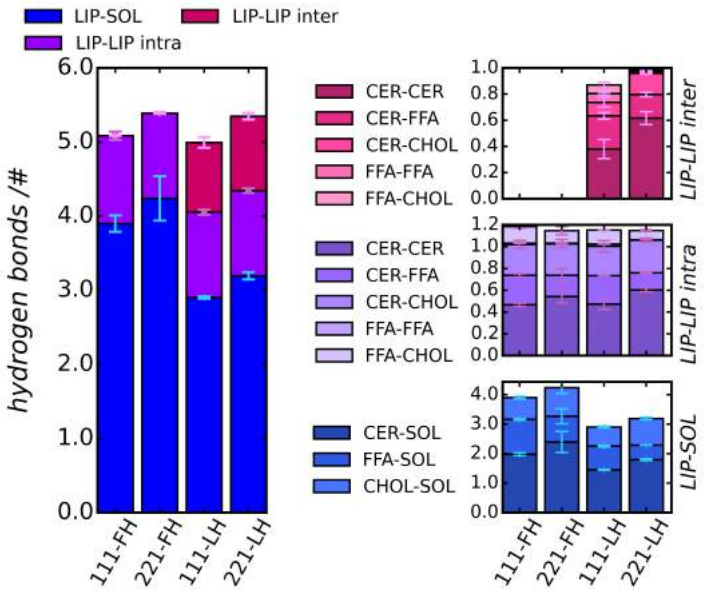

Fig. 5 Left hand side: the total number of H-bonds for the FH and LH bilayers averaged over three independent samples. Blue bars represent H-bonds between lipid and water (LIP-SOL), violet bars the intra-layer H-bonds between lipids (LIP-LIP intra) and the pink bars the inter-layer H-bonds between lipids (LIP-LIP inter). Right hand side: the contribution of CER[NS]24, CHOL and FFA24 to each H-bond network. No CHOL-CHOL H-bonds were found in any of the systems.

CER[NS]24-CER[NS]24 H-bonds are the most significant, which is to be expected given the greater number of H-bond donor and acceptor groups within the headgroup of CER[NS]24 compared to CHOL or FFA24.

3.4 Lateral Distribution of Water

As noted above, under conditions of low hydration small water pools form on the bilayer, where water covers about 75% of the surface and the remainder is characterised by dry regions where the lipid headgroups of adjacent bilayers are in contact. The 2D number density map of the inter-layer water for a selected LH 1:1:1 bilayer is shown in Figure 4. The black rectangles highlight areas of low thickness, which correspond to the dry regions of the bilayer. It is clear that the presence of these small pools of water affects the order and orientation of the lipids, leading to the thickness variations observed in all the LH samples.

To further explore the behaviour of the water pools over time and assess the effect of the system size on the shape of the pools, we prepared a larger 1:1:1 LH system, comprising 1440 lipids (720 lipids per bilayer) and simulated it for 425 ns. Snapshots of the system after 25 ns (same total simulation time as the small bilayers) and 425 ns are shown in Figure 6.

The 2D number density maps of the water are also reported. After 25 ns, most of the water molecules have clustered together and distinct wet and dry regions have started to form. By 425 ns, the pools have assumed a more compact shape, with the majority of water molecules belonging to flattened, isolated vesicles between the bilayers. A comparison between the water pools observed in the large and small bilayers is shown in Figure S25. The water pools in both systems have an approximately circular cross-sectional area and have a similar relative diameter. This confirms that pool formation is not a finite size artefact of the small system. For clarity, the periodic image of the larger 1:1:1 LH system at 425 ns is provided in Figure S26. By observing both Figure 6 and Figure S26 it is possible to notice how the pools affect the thickness of the system: areas which have water pools on both sides of the bilayer tend to have a higher thickness (∼5.0 nm) compared with areas that alternate dry and wet regions (∼4.0 nm). This is supported by 2D thickness maps (Figure 4 and S20-S24). We also found that lipids in the LH systems have, on average, higher tilting angles than lipids in the FH systems (Table S3). We suggest that the inter-layer H-bonding in the dry regions alters the conformation of the lipids so that they are more tilted, leading to a lower bilayer thickness.

The water pools in our simulations resemble, albeit on a much smaller scale, water pools reported experimentally for samples of highly hydrated real skin[26]. The formation of localised pools has also been seen in simulations of fatty acid multilayers where

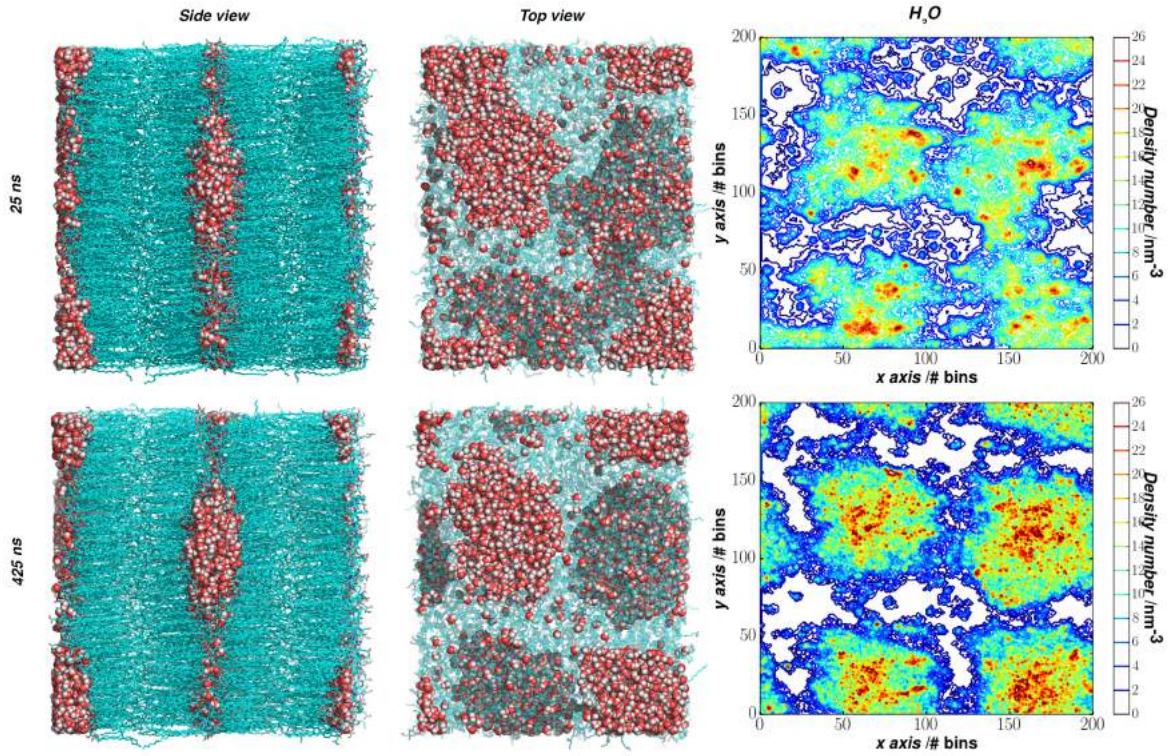

Fig. 6 Snapshots of the larger 1:1:1 LH system after 25 ns and 425 ns of MD simulation at 1 bar and 305 K. From the top: left hand side, side view; centre, top view; and right hand side, 2D number density map of water for the bilayer after 25 ns. From the bottom: left hand side, side view; centre, top view; and right hand side, 2D number density map of water for the bilayer after 425 ns. Carbon is coloured in cyan, oxygen in red, hydrogen in white and nitrogen in blue.

water-pool formation was shown to be driven by the entropy change associated with increasing the disorder of water and the reduction in interfacial tension with the lipids[34]. Water pooling was also observed in coarse-grained simulations of ceramide NS at 300 K[72]. The pooling of water between the lamellar sheets implies that there is no continuous aqueous phase in the SC. This may be of great significance for skin barrier function as it suggests that the presence of a lateral polar pathway is highly unlikely. Therefore a molecule that has diffused through a bilayer and reached the next layer of lipid headgroups is faced with additional energetic barriers in the lateral direction associated with transitions between pools and dry regions.

3.5 Water Permeation

Fully hydrated bilayers: To evaluate the permeation of a water molecule along the pathway normal to the 1:1:1 FH bilayer, the PMF for a water molecule moving from bulk water to the COM of the bilayer was calculated. To take into account the lateral heterogeneity of lipids in the bilayer, nine independent PMF profiles were calculated, corresponding to different locations of the water molecule in the xy plane. The averaged PMF profile and diffusion constants at each position are shown in the top and bottom of Figure 7a respectively. The same graph is reported against the density profile in Figure S27. As the water molecule moves through bulk water the PMF is at a plateau, at its minimum value. At a distance of 2.2 nm from the COM, which corresponds to the interface region between the water and the bilayer, the PMF starts to increase. At this location, there will be a balance of favourable lipid-water interactions such as H-bonding (discussed earlier) and an energetic penalty associated with desolvation of the water molecule and disruption of interactions between lipid headgroups. As the water molecule proceeds towards the COM of the bilayer, an energy barrier of $\sim$30 kJ mol^{-1} is found at a distance of 1.7 nm from the COM of the bilayer. This region corresponds to the most dense lipidic region of the system (Figure S27) and thus the most hydrophobic one. At the COM there is a local minimum of $\sim$10 kJ mol^{-1}; here the lipids tails are less dense (Figure S27), leading to a more favourable environment for the water molecule.

The diffusion coefficients follow the inverse trend to the PMF profile; we find that $D(z)$ is at a minimum in the most dense lipidic region (4.8×10^{-6} cm^2 s^{-1}) and increases at the COM (2.3×10^{-5} cm^2 s^{-1}). We estimate a resistance R_m of the FH 1:1:1 bilayer of 3.1×10^9 s cm^{-2} and a P of 3.3×10^{-10} cm^2 s^{-1}. Overall our results are in good agreement with previous computational work. The height of the barrier for a water molecule crossing the 1:1:1 FH bilayer is smaller than the barrier reported for pure CER bilayers[37]; however this is to be expected given the presence of CHOL, which is known to increase the degree of disorder in the bilayer and increase the free volume of the membrane[37]. Das et al.[37] found that the permeability of a 2:2:1 FH bilayer increased by approximately two orders of magnitude going from 300 K to 350 K. They only studied the 1:1:1 FH bilayer at the higher temperature and estimated a permeability of

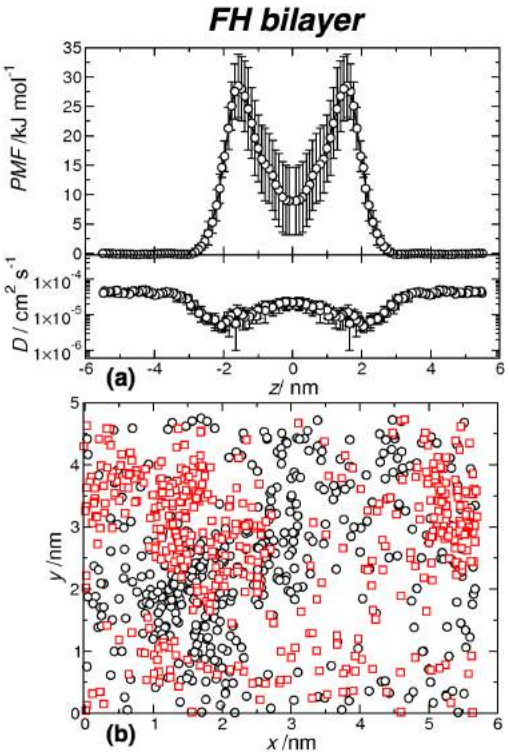

Fig. 7 (a) Average PMF profile and diffusion coefficients for a water molecule at a given depth along the FH 1:1:1 bilayer at 305 K. z = 0 corresponds to the bilayer mid-plane. The error bars show the standard deviation obtained from nine independent samples. (b) Independent trajectory of two water molecules (shown in black and red) placed at the COM of the 1:1:1 FH bilayer.

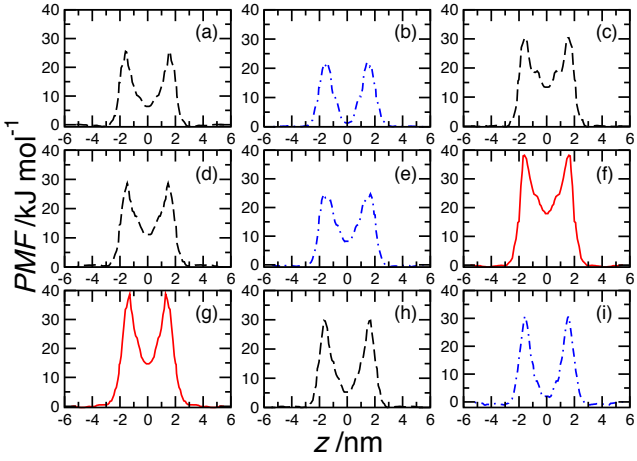

Fig. 8 PMF profiles for 9 independent water molecules placed at different initial xy positions into the 1:1:1 FH bilayer. $z = 0$ corresponds to the bilayer mid-plane. The relative error was smaller than 2%, thus for clarity, error bars are not shown. CHOL-rich pathways are shown in a dot-dashed blue line, interface regions between CHOL-rich and FFA-rich regions are shown in a continuous red line and intermediate compositions are shown in a dotted black line. The lipid composition for each profile, resistance and permeability coefficients are reported in Table S4.

8.2×10^{-8} cm^2 s^{-1}, which is about two orders of magnitude higher than the permeability of the 1:1:1 FH bilayer computed in this study at 305 K. The permeability calculated here is significantly lower than the permeability of human skin determined experimentally ($\sim 10^{-7}$ cm^2 s^{-1})[24]; this is probably due to the high polydispersity of human SC and the presence of some unsaturated lipid tails, which introduce a greater disorder in the lamellae. The permeability of water in our model is approximately eight orders of magnitude lower than that of a water molecule in a DPPC bilayer in the fluid phase determined by MD simulations[62].

As there is a heterogeneous distribution of lipids in the FH bilayers, a more detailed analysis of each independent PMF profile was performed to determine the influence of the local lipid environment on the permeation of water. The individual PMFs are shown in Figure 8 and the lipid composition in the region surrounding the permeating water molecule for each given profile is reported in Table S4.

Depending on the local lipid composition of the region traversed by the water molecule, the height of the free energy barrier ranges from 22 kJ mol^{-1} (Figure 8b) to 38 kJ mol^{-1} (Figure 8g). The variations in the PMF correspond to changes in composition of the bilayer at a given permeation region (Table S4). The profiles with the highest energy barrier (Figures 8f and g) correspond to regions in the membrane, with a relatively high concentration of FFA24 (50% and 37.5% respectively). A lower barrier is observed in regions with a high concentration of CHOL (Figures 8b, e and i). The variation in composition also leads to changes of up to 3 orders of magnitude in the permeability and resistance coefficients (Table S4). Our results suggest that the most favourable permeation pathways for water molecules in skin-lipid bilayers are through CHOL-rich regions.

The standard model of molecule permeation across the SC describes a tortuous pathway through the lipids, which includes diffusion in both the lateral and perpendicular directions. Therefore in building up our picture of skin transport, we must also consider the lateral pathways. The lateral diffusion coefficient of a water molecule at the COM of the bilayer, calculated with the Einstein relation, was found to be 1.3×10^{-5} cm^2 s^{-1}, which is the same order of magnitude for diffusion at the COM of the bilayer along the normal pathway. In Figure 7b, the trajectories of two water molecules placed at the COM of the 1:1:1 FH bilayer are shown in black and red. It is clear that at this depth the molecules are fairly free to move in the xy directions. In an hypothetical scenario where a water molecule has reached the COM by permeating along the normal direction to the bilayer, it is very likely that lateral diffusion will occur, allowing the water molecule to explore the xy plane and chance upon the most favourable pathway to exit the bilayer.

3.5.1 The low hydration bilayer

To evaluate the permeation of a water molecule along the pathway normal to the 1:1:1 LH bilayer, we calculated the PMF for a water molecule moving from the COM of one bilayer to the COM of the other. The PMF was collected for nine independent water molecules with different initial xy coordinates. By comparing

the position of the permeant to the position of the water pool, profiles were then assigned as being through a wet or a dry region. The averaged PMF for seven and two independent water molecules permeating through wet and dry regions respectively are shown as black and red lines at the top of Figure 9a. A value of zero was assigned to the PMF though a water pool (black line) at the interface between adjacent bilayers (z = 0) and the PMF profile through a dry region (red line) was shifted so that the absolute value of the PMF was the same at the COM of the bilayer for both profiles. The average diffusion coefficients are shown at the bottom of Figure 9a. The same graph is reported against the density profile in Figure S28. The PMFs for independent water molecules are not shown as we did not observe lateral demixing of lipids in the LH bilayer on the timescale of our simulations (the lipid composition around each permeating water is provided in Table S5); however if lipid phase separation also occurs in the LH system at longer timescales we would expect the shape of the contributing profiles to be influenced by the local lipid composition.

The PMF profiles for a water molecule through wet and dry regions have a very similar shape, suggesting that overall the barrier properties of the LH bilayer are not strongly affected by the presence of the pool. At the COM there is a minima in both profiles, similar to that observed for the FH bilayer. The PMF at this depth is equal to 22 kJ mol^{-1}. At a distance of ∼1.3 nm from the COM, an energy barrier is found, where the lipidic region is more dense (∼27 and 25 kJ mol^{-1} for the wet and dry profiles respectively). The ΔG between the lipidic region and the COM is ∼5 and 3 kJ mol^{-1} for the wet and dry profile respectively, lower than the energy barrier observed in the FH bilayer. This suggests that movement of water from the COM to the headgroup region is more favourable at low hydration. The total ΔG between the interface region (z = 0) and the highest point in the barrier is still relatively high (∼27 and 23 kJ mol^{-1} for the wet and dry profiles respectively), thus permeation of a water molecule found at the interface is still improbable. Previous studies of water permeation through a dehydrated skin-lipid bilayer have reported a free energy barrier of ∼30 kJ mol^{-1} to cross the interface and an overall ΔG of ∼10 kJ mol^{-1} for a water molecule moving from the COM of one bilayer to the barrier[38], which is larger than those observed in our model (∼5 and 3 kJ mol^{-1}). This suggests that a lower concentration of water increases the disorder in the bilayer and leads to slightly more permeable lamellae.

The diffusion profiles of water in the LH bilayer are shown in the bottom of Figure 9a. As with the PMF profiles, the diffusion profiles for wet and dry regions are similar to each other. Unlike the FH bilayer, the diffusion does not show a clear dependence on the z position in the bilayer although the diffusion in the centre of the bilayer is similar for both FH and LH systems. The permeability obtained for the wet and dry regions are 1.7 × 10^{-10} and 5.3 × 10^{-9} cm^2 s^{-1} respectively, with corresponding resistances of 6.0 × 10^9 and 1.9 × 10^8 s cm^{-2}. Dry regions seem to be more permeable than wet regions, which this suggests that the presence of water pools in the SC does not facilitate permeation but rather hydrophilic molecules may become trapped in the pool and consequently are less likely to permeate the adjacent bilayer.

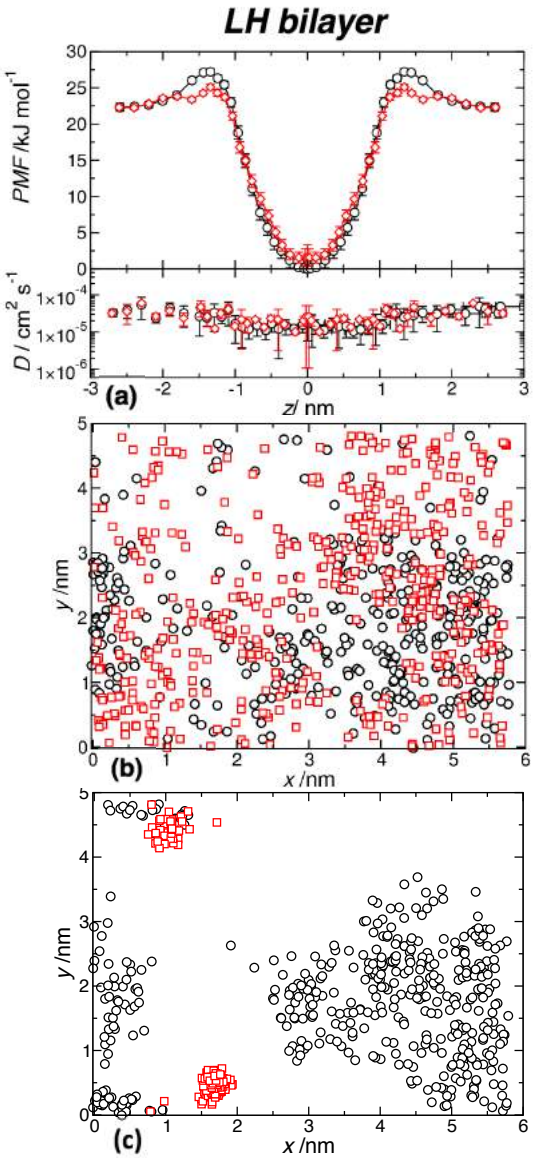

Fig. 9 (a) Average PMF profile and diffusion coefficients for a water molecule at a given depth along the LH 1:1:1 bilayer at 305 K. z = 0 corresponds to the interface region between adjacent bilayers. The black and red lines represent the PMF profile through wet and dry regions respectively. The error bars show the standard deviation obtained from seven (PMF profile along a wet region) and two (PMF profile along a dry region) independent samples. (b) Independent trajectory of two water molecules (shown in black and red) placed at the COM of the 1:1:1 LH bilayer. (c) Independent trajectory of two water molecules (shown in black and red) placed at the interface region between two adjacent bilayers in the 1:1:1 LH bilayer.

The trajectories of two independent water molecules placed at the COM of the 1:1:1 LH bilayer are shown in black and red in Figure 9b while the trajectories of two independent water molecules placed at the interface region between adjacent bilayers are shown in Figure 9c. Similar to what we observed for the 1:1:1 FH bilayer, a water molecule placed at the COM is fairly free to move in the xy direction, with a diffusion equal to 1.2 × 10^{-5} cm^2 s^{-1}.

For a water molecule in the pool (black circles), we found a diffusion of 0.9×10^{-5} cm^2 s^{-1}, slightly lower than diffusion at the COM. In this environment the molecule diffuses freely within the pool but does not exit the pool. When a water molecule is found in the dry region (red rectangles), the diffusion decreases by almost two orders of magnitude (0.9×10^{-6} cm^2 s^{-1}) and, as shown by the trajectory in Figure 9c, almost no lateral diffusion is observed. Thus, a water molecule at the dry interface between adjacent bilayers will most likely form H-bonds with the lipid headgroups in that region and the lateral diffusion will be inhibited by both the lack of free volume and the H-bond network. In a hypothetical scenario where a water molecule has permeated a SC lamellae and is located at a dry interface between two adjacent bilayers, lateral permeation along the lipid headgroup region will be extremely unlikely.

4 Conclusion

Identification and characterisation of permeation pathways through complex lipid systems is crucial for developing strategies to control the transport of foreign molecules in these environments. In this work we have reported MD simulations of skin-lipid bilayers representative of the SC lipid lamellae at different lipid compositions (CER[NS]24:CHOL:FFA24 ratios of 1:1:1 and 2:2:1) and levels of hydration. Our key findings from these simulations are: (i) in FH systems, the lipids do not form a homogeneous mixture, rather we observe the formation of laterally CHOL-rich and CHOL-depleted regions (we suggest that in LH systems this lateral phase separation is inhibited by the formation of inter-layer H-bonds but that it may occur on longer timescales than are accessible to our simulations); and (ii) in LH systems, where the water concentration is closer to that of real skin, the water forms distinct flattened ellipsoid-shaped pools between the layers and therefore there is no continuous water layer in the SC. Based on our observations we have proposed a number of possible permeation pathways through the SC, both in the lateral and perpendicular membrane directions, through regions of different local lateral lipid composition and through water pools or dry areas, and conducted extensive permeability studies by means of potential of mean constraint force and diffusion calculations. First, considering transport in the perpendicular direction, the results revealed that permeation of water is more favourable through the CHOL-rich regions of the bilayers, which may be due to the increased free volume found around CHOL molecules in skin-lipid bilayers[36]. For a water molecule crossing the interface, permeation through a dry region is more probable than through a water pool. Second, considering lateral transport, we found water had the highest diffusion coefficient when it was located within the lower-density lipidic region at the COM of the bilayer. In the headgroup region, water was able to diffuse quite rapidly within a water pool but was unlikely to escape the pool, and in the dry regions water became trapped and lateral diffusion coefficients were reduced by 1-2 orders of magnitude. Bringing this together, we propose that in a scenario where a water or other small hydrophilic molecule is crossing the SC, slow permeation will occur along the most energetically favourable CHOL-rich and/or dry pathways in the direction normal to the bilayer (Figure 10, pathway A) while relatively fast lateral diffusion will take place at the COM of the bilayers (Figure 10, pathway B). We suggest that lateral permeation within the bilayer increases the probability of the permeant encountering a CHOL-rich region through which to exit the bilayer.

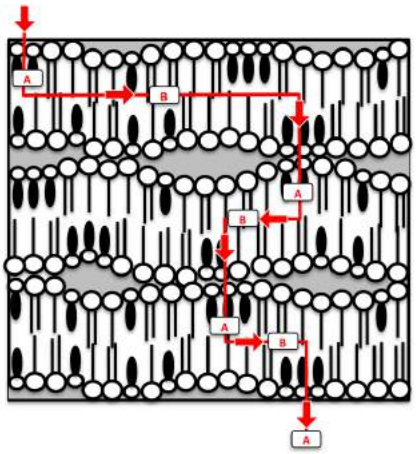

Fig. 10 Suggested pathway for the permeation of a small polar molecule across the SC lipid lamellae. Lipids are represented schematically: CER[NS]24 and FFA24 are represented by circles with two and one tail(s) respectively; CHOL is represented by a small circle and solid ellipse. Pathway A corresponds to the slow permeation along the most energetically favourable CHOL-rich and dry regions and pathway B corresponds to the fast diffusion along the bilayer COM.

Acknowledgement

The authors acknowledge the European Chemical Industry Council (CEFIC) for funding this project and computing resources provided by the Scientific Computing Research Technology Platform at the University of Warwick. We thank Dr Russell DeVane and Dr David Bray for useful discussions during the preparation of this manuscript. RN thanks the Royal Society for a University Research Fellowship.

References

1 A. S. Michaels, S. K. Chandrasekaran and J. E. Shaw, *AIChE Journal*, 1975, **21**, 985–996.

2 J. A. Bouwstra, F. E. Dubbelaar, G. S. Gooris and M. Ponec, *Acta Derm. Venereol. Suppl.*, 2000, **208**, 23–30.

3 P. Krieg and G. Fürstenberger, *BBA - Mol. Cell Biol. L.*, 2014, **1841**, 390–400.

4 D. Groen, G. S. Gooris and J. A. Bouwstra, *Biophys. J.*, 2009, **97**, 2242–2249.

5 D. Groen, G. S. Gooris, D. J. Barlow, M. J. Lawrence, J. B. van Mechelen, B. Demé and J. A. Bouwstra, *Biophys. J.*, 2011, **100**, 1481–1489.

6 M. N. A. Ansari, N. Nicolaides and H. C. Fu, *Lipids*, 1970, **5**, 838–845.

7 H. Farwanah, K. Raith, R. H. Neubert and J. Wohlrab, *Arch. Dermatol. Res.*, 2005, **296**, 514–521.

8 L. Norlén, I. Nicander, A. Lundsjö, T. Cronholm and B. Forslind, *Arch. Dermatol. Res.*, 1998, **290**, 508–516.

9 J. van Smeden, M. Janssens, G. S. Gooris and J. A. Bouwstra, *BBA - Mol. Cell Biol. L.*, 2014, **1841**, 295–313.

10 J. Bouwstra, G. Pilgram, G. Gooris, H. Koerten and M. Ponec, *Skin Pharmacol. App. Skin Physiol.*, 2001, **14**, 52–62.

11 J. Bouwstra, Y. Grams, G. Pilgram and H. Koerten, *Microsc. Microanal.*, 2002, **8**, 278–279.

12 E. H. Mojumdar, D. Groen, G. S. Gooris, D. J. Barlow, M. J. Lawrence, B. Deme and J. A. Bouwstra, *Biophys. J.*, 2013, **105**, 911–918.

13 E. H. Mojumdar, Z. Kariman, L. van Kerckhove, G. S. Gooris and J. A. Bouwstra, *BBA - Biomembranes*, 2014, **1838**, 2473–2483.

14 J. A. Bouwstra, G. S. Gooris, F. E. R. Dubbelaar and M. Ponec, *J. Lipid Res.*, 2001, **42**, 1759–1770.

15 K. W. Ng and W. M. Lau, in *Skin Deep: The Basics of Human Skin Structure and Drug Penetration*, ed. N. Dragicevic and I. H. Maibach, Springer Berlin Heidelberg, Berlin, Heidelberg, 2015, pp. 3–11.

16 B. Forslind, *Acta Derm. Venereol.*, 1994, **74**, 1–6.

17 A. Percot and M. Lafleur, *Biophys. J.*, 2001, **81**, 2144–2153.

18 L. Norlén, I. P. Gil, A. Simonsen and P. Descouts, *J. Struct. Biol.*, 2007, **158**, 386–400.

19 G. L. Nicolson, *BBA - Biomembranes*, 2014, **1838**, 1451–1466.

20 H. I. Ingólfsson, M. N. Melo, F. J. van Eerden, C. Arnarez, C. A. Lopez, T. A. Wassenaar, X. Periole, A. H. de Vries, D. P. Tieleman and S. J. Marrink, *J. Am. Chem. Soc.*, 2014, **136**, 14554–14559.

21 V. D. Gordon, T. J. O'Halloran and O. Shindell, *Phys. Chem. Chem. Phys.*, 2015, **17**, 15522–15533.

22 R. R. Warner, M. C. Myers and D. A. Taylor, *J. Invest. Dermatol.*, 1988, **90**, 218–224.

23 E. Sparr, D. Millecamps, M. Isoir, V. Burnier, Å. Larsson and B. Cabane, *J. R. Soc. Interface*, 2013, **10**, 20120788.

24 I. H. Blank, J. Moloney, A. G. Emslie, I. Simon and C. Apt, *J. Invest. Dermatol.*, 1984, **82**, 188–194.

25 C. L. Silva, D. Topgaard, V. Kocherbitov, J. J. S. Sousa, A. A. C. C. Pais and E. Sparr, *BBA - Biomembranes*, 2007, **1768**, 2647–2659.

26 J. A. Bouwstra, A. de Graaff, G. S. Gooris, J. Nijsse, J. W. Wiechers and A. C. van Aelst, *J. Invest. Dermatol.*, 2003, **120**, 750–758.

27 G. Tan, P. Xu, L. B. Lawson, J. He, L. C. Freytag, J. D. Clements and V. T. John, *J. Pharm. Sci.*, 2010, **99**, 730–740.

28 J. Torin Huzil, S. Sivaloganathan, M. Kohandel and M. Foldvari, *Wiley Interdiscip. Rev. Nanomed. Nanobiotechnol.*, 2011, **3**, 449–462.

29 R. Notman and J. Anwar, *Adv. Drug Deliver. Rev.*, 2013, **65**, 237–250.

30 D. W. O'Neill, S. Y. Noh and R. Notman, in *Computer Simulations of Lipid Membranes and Liposomes for Drug Delivery*, John Wiley & Sons, Ltd, 2015, pp. 101–122.

31 S. A. Pandit and H. L. Scott, *J. Chem. Phys.*, 2006, **124**, 014708.

32 R. Notman, W. K. den Otter, M. G. Noro, W. J. Briels and J. Anwar, *Biophys. J.*, 2007, **93**, 2056–2068.

33 M. Höltje, T. Förster, B. Brandt, T. Engels, W. von Rybinski and H.-D. Höltje, *BBA - Biomembranes*, 2001, **1511**, 156–167.

34 C. M. MacDermaid, R. H. DeVane, M. L. Klein and G. Fiorin, *J. Chem. Phys.*, 2014, **141**, 22D526.

35 K. R. Hadley and C. Mc Cabe, *Soft Matter*, 2012, **8**, 4802–4814.

36 C. Das, M. G. Noro and P. D. Olmsted, *Biophys. J.*, 2009, **97**, 1941–1951.

37 C. Das, P. D. Olmsted and M. G. Noro, *Soft Matter*, 2009, **5**, 4549–4555.

38 C. Das, M. G. Noro and P. D. Olmsted, *Soft Matter*, 2014, **10**, 7346–7352.

39 C. Das, M. G. Noro and P. D. Olmsted, *Phys. Rev. Lett.*, 2013, **111**, 148101.

40 C. Das and P. D. Olmsted, *Phil. Trans. R. Soc. A*, 2016, **374**,.

41 M. Paloncýová, K. Vávrová, ť. Sovová, R. DeVane, M. Otyepka and K. Berka, *J. Phys. Chem. B*, 2015, **119**, 9811–9819.

42 I. Iwai, H. Han, L. den Hollander, S. Svensson, L.-G. ÖŰfverstedt, J. Anwar, J. Brewer, M. Bloksgaard, A. Laloeuf, D. Nosek, S. Masich, L. A. Bagatolli, U. Skoglund and L. Norlén, *J. Invest. Dermatol.*, 2012, **132**, 2215–2225.

43 R. Thind, D. W. O'Neill, A. Del Regno and R. Notman, *Chem. Commun.*, 2015, **51**, 5406–5409.

44 R. Notman, J. Anwar, W. Briels, M. G. Noro and W. K. den Otter, *Biophys. J.*, 2008, **95**, 4763–4771.

45 M. I. Hoopes, M. G. Noro, M. L. Longo and R. Faller, *J. Phys. Chem. B*, 2011, **115**, 3164–3171.

46 A. Akinshina, C. Das and M. G. Noro, *Phys. Chem. Chem. Phys.*, 2016, **18**, 17446–17460.

47 M. Paloncýová, R. H. DeVane, B. P. Murch, K. Berka and M. Otyepka, *Langmuir*, 2014, **30**, 13942–13948.

48 W. D. Bennett and D. P. Tieleman, *BBA - Biomembranes*, 2013, **1828**, 1765–1776.

49 O. Berger, O. Edholm and F. Jähnig, *Biophys. J.*, 1997, **72**, 2002–2013.

50 W. L. Jorgensen and J. Tirado-Rives, *J. Am. Chem. Soc.*, 1988, **110**, 1657–1666.

51 J.-P. Ryckaert and A. Bellemans, *Chem. Phys. Lett.*, 1975, **30**, 123–125.

52 H. Berendsen, J. Postma, W. van Gunsteren and J. Hermans, *B. Pullman (Ed.), Intermolecular Forces, Reidel, Dordrecht, The Netherlands*, 1981, 331–342.

53 D. van Spoel, E. Lindahl, B. Hess, A. R. van Buuren, E. Apol, P. J. Meulenhoff, D. P. Tieleman, A. L. T. M. Sijbers, K. A. Feenstra, R. van Drunen and H. J. C. Berendsen, *Gromacs User Manual version 4.5.4, www.gromacs.org (2010)*.

54 P. M. and R. A., *J. Appl. Phys.*, 1981, **52**, 7182–7190.

55 N. S. and K. M. L., *Mol. Phys.*, 1983, **50**, 1055–1076.

56 T. Darden, D. York and L. Pedersen, *J. Chem. Phys.*, 1993, **98**, 10089âĂŞ10092.

57 U. Essmann, L. Perera, M. L. Berkowitz, T. Darden, H. Lee and L. G. Pedersen, *J. Chem. Phys.*, 1995, **103**, 8577–ĂŞ8592.

58 B. Hess, H. Bekker, H. J. C. Berendsen and J. G. E. M. Fraaije, *J. Comput. Chem.*, 1997, **18**, 1463–1472.
59 S. Miyamoto and P. A. Kollman, *J. Comput. Chem.*, 1992, **13**, 952–962.
60 S. J. Marrink and H. J. C. Berendsen, *J. Phys. Chem.*, 1994, **98**, 4155–4168.
61 S. J. Marrink and H. J. C. Berendsen, *J. Phys. Chem.*, 1996, **100**, 16729–ĹŠ16738.
62 D. Bemporad, J. W. Essex and C. Luttmann, *J. Phys. Chem. B*, 2004, **108**, 4875–4884.
63 D. Bemporad, C. Luttmann and J. Essex, *Biophys. J.*, 2004, **87**, 1–13.
64 M. Orsi and J. W. Essex, *Soft Matter*, 2010, **6**, 3797–3808.
65 M. P. Allen and D. J. Tildesley, *Computer Simulations of Liquids*, Oxford: Oxford Science Publications, 1987.
66 V. Gapsys, B. L. de Groot and R. Briones, *J. Comput. Aid. Mol. Des.*, 2013, **27**, 845–858.
67 V. K. Sharma, E. Mamontov, D. B. Anunciado, H. O'Neill and V. S. Urban, *Soft Matter*, 2015, **11**, 6755–6767.
68 X. Xu and E. London, *Biochemistry*, 2000, **39**, 843–849.
69 X. Lin, J. H. Lorent, A. D. Skinkle, K. R. Levental, M. N. Waxham, A. A. Gorfe and I. Levental, *J. Phys. Chem. B*, 2016, **120**, 11930–11941.
70 C. Paré and M. Lafleur, *Langmuir*, 2001, **17**, 5587–5594.
71 J. Ouimet and M. Lafleur, *Langmuir*, 2004, **20**, 7474–7481.
72 Ž. Sovová, K. Berka, M. Otyepka and P. Jurečka, *J. Phys. Chem. B*, 2015, **119**, 3988–3998.